IEEE Access
Multidisciplinary | Rapid Review | Open Access Journal

Received 19 August 2022, accepted 12 September 2022, date of publication 16 September 2022,
date of current version 26 September 2022.

Digital Object Identifier 10.1109/ACCESS.2022.3207159

RESEARCH ARTICLE

A Cylindrical Equivalent Source-Based Physical Optics Method for Rapid Analysis of Airborne Radomes

XIANJUN SHENG[1], YE ZHANG[1], RUI SHEN[2], AND NING LIU[1]
[1]School of Electrical Engineering, Dalian University of Technology, Dalian 116024, China
[2]China Academy of Launch Vehicle Technology, Beijing 100076, China

Corresponding author: Ning Liu (liun@dlut.edu.cn)

This work was supported in part by the National Natural Science Foundation of China under Grant 52005079 and Grant 52075069, and in part by the Fundamental Research Funds for the Central Universities under Grant DUT21RC(3)069.

ABSTRACT The physical optics (PO) method treats the outer surface of airborne radomes in front of antennas as a secondary source region when analyzing the electromagnetic performance. The effective reduction of the secondary source region can significantly improve the computational efficiency, which is helpful for the rapid analysis and design of airborne radomes. In this paper, we present a cylindrical equivalent source-based PO method by introducing an antenna radiation cylinder that can cover the main near-field radiation characteristics of the antenna. The cubic-spline interpolation technique is used to standardize the solution method for the boundary of the cylindrical equivalent source of different antenna-radome systems. The results of a tangent-ogival radome verify the validity of the proposed method. Compared with the conical equivalent source-based PO method, the proposed method improves the efficiency by 71.83%. It can be applied to airborne antenna-radome systems with antenna diameters of 12.14 times of wavelength and above, using 10% as the error threshold.

INDEX TERMS Airborne radomes, cubic-spline interpolation, cylindrical equivalent source, physical optics method.

I. INTRODUCTION

Airborne radomes are dielectric shells that enclose antenna systems for protection. However, the existence of airborne radomes worsens the radiation characteristics of antennas, causing transmission loss (TL) and boresight error (BSE) [1], [2], [3]. Such deteriorations in radiation characteristics restrict the application of high-performance antennas in aircraft applications. Hence, numerical methods are necessary to evaluate the influence of radomes on the antenna performance.

Currently, these methods can be divided into three categories: 1) low-frequency (LF) methods represented by the method of moments (MoM) [4] and the finite element method (FEM) [5], 2) high-frequency (HF) methods represented by the geometric optics (GO) method [6] and the physical optics (PO) method [7], [8], and 3) hybrid HF/LF methods represented by the hybrid PO-MoM technique [9]. Note that the LF methods have the highest accuracy. However, they are usually used for electrically small antenna-radome systems, owing to the limitations of high computer memory requirements and longtime consumption. Compared with the LF methods, the hybrid HF/LF methods exhibit improved efficiency. However, in the iterative optimization design process of radomes, the hybrid HF/LF methods are still time-consuming. The GO method in HF is concise and efficient. Unfortunately, its accuracy is uncertain due to the ray-tracing approximations of the antenna aperture fields [8]. Most of the airborne antenna-radome systems are electrically medium or large. For the analysis of such structures, the PO method in HF is a good choice in terms of both accuracy and efficiency.

In the past decades, many studies have been performed on the PO method. A PO approximation for the induced electric

The associate editor coordinating the review of this manuscript and approving it for publication was Byung-Gyu Kim.

and magnetic surface currents is proposed in [10] with the help of second-order boundary conditions on a special type of anisotropic thin dielectric layer. To achieve the uniform convergence of the surface integration at different operating frequencies, an adaptive grid technique is proposed in [11]. The calculation of the transmission coefficient in the PO method is improved by introducing a lateral phase factor [12]. The electromagnetic (EM) performance of a tangent-ogival radome is analyzed in [13] by applying the PO method. It can be easily deduced from the principle of the PO method that the calculations in the secondary source region consume most of the time. Therefore, a reasonable reduction of the secondary source region, namely, the definition of the equivalent source region, is the key to improving the efficiency of the PO method. Demetrius T. Paris proposes the idea of using an antenna radiation cone to define the equivalent source region [7]. Based on this idea, a conical equivalent source-based PO method is proposed in [14], which improves the computational efficiency of the PO method to some extent. However, other methods for defining the equivalent source region have not been reported. A more efficient PO method is desired for the rapid analysis and design of radomes.

To further improve the efficiency and facilitate the rapid analysis and design of radomes, a cylindrical equivalent source-based PO method is proposed in this paper. An antenna radiation cylinder based on the antenna aperture is established by analyzing the near-field radiation characteristics of the antenna. The outer surface of the radome inside the antenna radiation cylinder is then defined as the cylindrical equivalent source. In addition, the solution method for the boundary of the cylindrical equivalent source is generalized using the cubic-spline interpolation technique. This generalization allows the proposed method to be easily applied to different radomes. Compared with the conical equivalent source-based PO method, the proposed method can significantly improve the computational efficiency.

II. THEORETICAL BASIS AND REALIZATION METHOD OF CYLINDRICAL EQUIVALENT SOURCE

The PO method can be divided into three steps [15]: 1) The near fields incident on the inner surface of the radome are calculated from the antenna aperture fields. 2) The transmitted fields at the outer surface of the radome are calculated from the near fields using the local planar sheet approximation. 3) The transmitted fields are equivalent to the secondary sources, and the far fields are then calculated from the secondary sources. It can be deduced that the transmitted fields at different points on the outer surface of the radome have different intensities. In other words, some secondary source points have relatively large fields, whereas others have relatively small fields. It is expected that every secondary source point with a relatively large field should be included in the equivalent source region. Therefore, the equivalent source region should be defined only after studying the near-field radiation characteristics of the antenna.

A. THEORETICAL BASIS OF CYLINDRICAL EQUIVALENT SOURCE

It can be concluded from the derivation of vector potential formulation that the plane wave spectrum (PWS) theory and the aperture integration (AI) theory are equivalent for the near-field calculation of the antenna. The PWS expression of the electric field in the near-field zone for a y-polarized uniform circular aperture antenna is given by [15]:

$$\boldsymbol{E}(x,y,z)=\frac{1}{4\pi^2}\int_{-\infty}^{+\infty}\int_{-\infty}^{+\infty}\frac{1}{k_z}exp\left[-j(k_xx+k_yy+k_zz)\right]\cdot(\hat{\boldsymbol{y}}k_z-\hat{\boldsymbol{z}}k_y)\boldsymbol{F}(k_x,k_y)dk_xdk_y, \quad (1)$$

where (k_x, k_y, k_z) is the wavenumber vector, $\hat{\boldsymbol{y}}$ and $\hat{\boldsymbol{z}}$ are respectively the unit vectors along the y-axis and z-axis, and $\boldsymbol{F}(k_x, k_y)$ is the angular spectrum of plane waves obtained by the Fourier transform [15]:

$$\boldsymbol{F}(k_x,k_y)=\iint_S E_y(x',y')exp\left[j(k_xx'+k_yy')\right]dx'dy', \quad (2)$$

where S denotes the antenna aperture and $E_y(x', y')$ is the tangential component of the electric field at the antenna aperture.

A uniformly distributed y-polarized circular aperture antenna having a diameter of 14λ (wavelength) was used as the simulation object. The antenna coordinate system was established with the center of the antenna aperture as the origin. The electric fields were calculated in the xoz plane for a series of observation points (x) on the observation plane at $z = 4\lambda$, 16λ, and 64λ, respectively, as shown in Fig. 1.

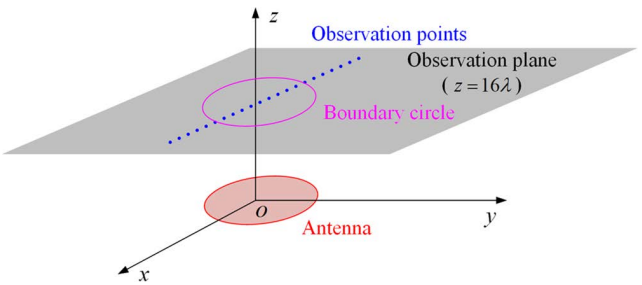

FIGURE 1. Observation points on the observation plane in the antenna coordinate system.

The calculated results for the electric fields are illustrated in Fig. 2. It can be seen that the electric field intensity is related to the observation plane distance (i.e., the distance from the observation plane to the antenna aperture, z) and the observation point distance (i.e., the distance from the observation point to the z-axis, x). When the observation plane distance increases, the main lobe of the antenna gradually forms. The observation points on the main lobe have relatively large fields, playing a crucial role in the far fields of the antenna. On the observation plane, a circle with a suitable radius centered on the antenna axis (z-axis) is drawn. This circle is referred to as the boundary circle, as shown in Fig. 1 and Fig. 2. The field of the observation point outside

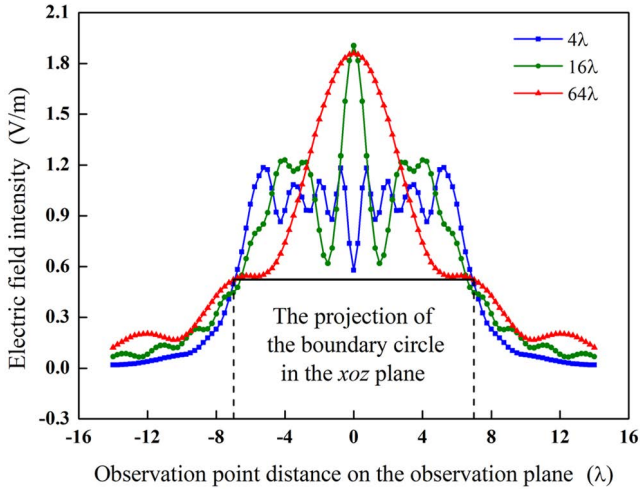

FIGURE 2. Near-field radiation characteristics of the antenna.

the boundary circle is relatively small, and tends to decrease as the observation point distance increases. The observation points outside the boundary circle contribute less to the far fields than those inside the boundary circle. According to this characteristic, it is unnecessary to treat the entire outer surface of the radome in front of the antenna as the secondary source region. It only requires defining the equivalent source region based on the contribution of the point on the outer surface of the radome to the far fields. Naturally, the radius of the antenna aperture can be used as the radius of the boundary circle. That is, the suitable radius of the boundary circle in this case is 7λ. This provides a theoretical basis for defining the equivalent source region using an antenna radiation cylinder.

B. REALIZATION METHOD OF CYLINDRICAL EQUIVALENT SOURCE

Fig. 3 illustrates the geometry of the antenna-radome system where (x_r, y_r, z_r) is the radome coordinate system with origin o_r situated at the center of the radome base, and (x, y, z) is the antenna coordinate system with origin o situated at the center of the antenna aperture.

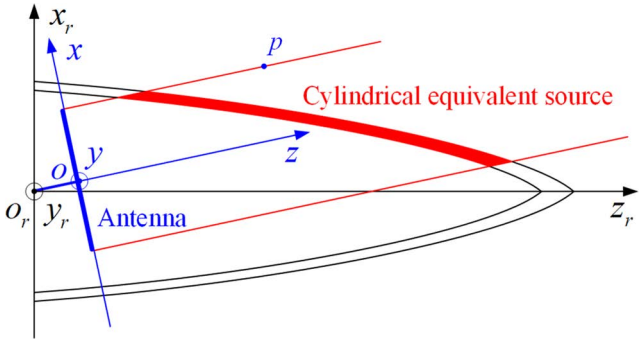

FIGURE 3. Geometry for the antenna-radome system.

In the antenna coordinate system, a cylinder with the antenna aperture as the bottom and perpendicular to the antenna aperture is built, which is denoted by the antenna radiation cylinder. The intersection of the antenna radiation cylinder with the outer surface of the radome determines the appropriate secondary source region. In other words, the outer surface of the radome contained within the antenna radiation cylinder is defined as the cylindrical equivalent source. The antenna radiation cylinder in the antenna coordinate system is expressed as:

$$\begin{cases} x = \rho\cos\theta \\ y = \rho\sin\theta \\ z = z, \end{cases} \tag{3}$$

where ρ is the distance from any point p on the antenna radiation cylinder to the z-axis and θ is the angle between the projection of line op in the xoy plane and the positive x-axis.

In general, airborne radomes are bodies of revolution with streamlined shapes. However, different shape equations require different solution methods when using the computer to solve the boundary of the cylindrical equivalent source. This brings a lot of trouble to programming. Therefore, the cubic-spline interpolation technique with the not-a-knot condition can be used to develop similar mathematical models for different radomes. These similar mathematical models can unify the solution method for the boundary of the cylindrical equivalent source. Compared with the clamped condition, the first-order derivatives at the endpoints are not required in the not-a-knot condition, which avoids the severe degradation of interpolation accuracy caused by the infinite first-order derivatives at the endpoints.

In the $x_r o_r z_r$ plane of the radome coordinate system, the cubic-spline interpolation of the radome generatrix is expressed as:

$$x_r = a_i + b_i(z_r - z_{ri}) + c_i(z_r - z_{ri})^2 + d_i(z_r - z_{ri})^3, \tag{4}$$

with

$$\begin{cases} a_i = x_{ri} \\ b_i = \dfrac{x_{ri+1} - x_{ri}}{z_{ri+1} - z_{ri}} - \dfrac{z_{ri+1} - z_{ri}}{2} m_i - \dfrac{z_{ri+1} - z_{ri}}{6}(m_{i+1} - m_i) \\ c_i = \dfrac{m_i}{2} \\ d_i = \dfrac{m_{i+1} - m_i}{6(z_{ri+1} - z_{ri})} \end{cases} \tag{5}$$

where (z_{ri}, x_{ri}) is the interpolation node on the radome generatrix and m_i is the second-order derivative at the i-th interpolation node.

The equation for the outer surface of the radome can be obtained by rotating the curve (4) with the z_r-axis as the symmetry axis:

$$\sqrt{x_r^2 + y_r^2} = a_i + b_i(z_r - z_{ri}) + c_i(z_r - z_{ri})^2 + d_i(z_r - z_{ri})^3. \tag{6}$$

To solve the boundary of the cylindrical equivalent source, the antenna radiation cylinder (3) is transformed into the

radome coordinate system [16]:

$$\begin{bmatrix} x_r \\ y_r \\ z_r \end{bmatrix} = \begin{bmatrix} 1 & 0 & 0 \\ 0 & \cos\omega & \sin\omega \\ 0 & -\sin\omega & \cos\omega \end{bmatrix} \begin{bmatrix} \cos\Omega & 0 & \sin\Omega \\ 0 & 1 & 0 \\ -\sin\Omega & 0 & \cos\Omega \end{bmatrix} \times \left(\begin{bmatrix} x \\ y \\ z \end{bmatrix} + \begin{bmatrix} 0 \\ 0 \\ \Delta_\Omega \end{bmatrix} \right), \quad (7)$$

where ω denotes the antenna scan angle in the azimuth plane, Ω denotes the antenna scan angle in the elevation plane, and Δ_Ω denotes the elevation offset.

The boundary of the cylindrical equivalent source can be solved by using the dichotomy method [17], after combining the outer surface of the radome (6) and the antenna radiation cylinder (7).

The transmitted fields in the cylindrical equivalent source region can be calculated using the near-field expression (1) and the local planar sheet approximation [15]. As in the traditional PO method, the surface integration method is applied to calculate the far fields:

$$\boldsymbol{E}(x_r, y_r, z_r) = \frac{-jk}{4\pi} \iint_{S_c} \left[\sqrt{\frac{\mu}{\varepsilon}} (\hat{\boldsymbol{n}} \times \boldsymbol{H}) - \left(\sqrt{\frac{\mu}{\varepsilon}} (\hat{\boldsymbol{n}} \times \boldsymbol{H}) \cdot \hat{\boldsymbol{r}} \right) \hat{\boldsymbol{r}} - \hat{\boldsymbol{r}} \times (\boldsymbol{E} \times \hat{\boldsymbol{n}}) \frac{exp(-jkr)}{r} \right] ds, \quad (8)$$

where S_c is the cylindrical equivalent source region; μ and ε are the permeability and permittivity in free space, respectively; $\hat{\boldsymbol{n}}$ is the unit outward normal vector to the radome surface; r is the distance from the origin to the far-field point (x_r, y_r, z_r) in the radome coordinate system; and $\hat{\boldsymbol{r}}$ is the unit vector along r.

When the far fields are obtained, the EM performance parameters, such as the far-field pattern, BSE, BSE slope (BSES), and power transmission (PT), can then be evaluated.

III. NUMERICAL SIMULATION AND EXPERIMENTAL VERIFICATION

A. EFFECTIVENESS OF THE CYLINDRICAL EQUIVALENT SOURCE-BASED PO METHOD

A tangent-ogival radome having a base diameter of 18λ [18] was used as the simulation object. The circular aperture antenna enclosed inside the radome has a diameter of 14λ and a y-polarized uniform aperture field. The antenna is mechanically scanned in the elevation plane from $-30°$ to $+30°$. Both methods proposed in this paper and [14] were used to compute BSE and BSES. The measurement was performed in a microwave anechoic chamber, as shown in Fig. 4. The measurement system is illustrated in Fig. 5. It is mainly composed of the transmitting section, the receiving section, and the control-processing section. The transmitting section consists of the transmitting port of the vector network analyzer (VNA), the power amplifier, the directional coupler, and the transmitting antenna. The receiving section includes the radome, the receiving antenna, and the receiving port of the VNA. The control-processing section contains the pillar, the gimbal, the gimbal controller, the rotary table, the rotary table controller, and the computer.

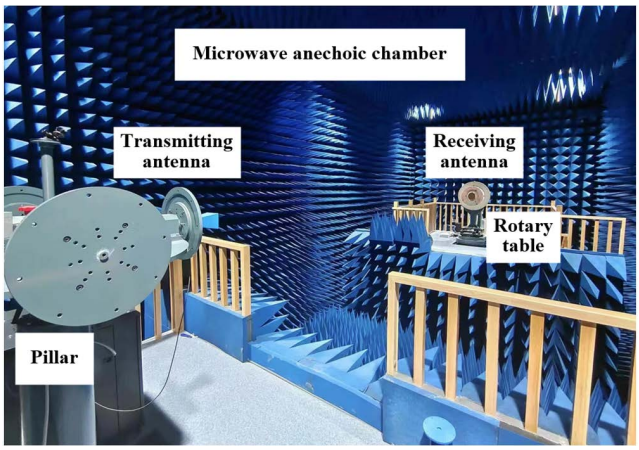

FIGURE 4. Environment and platform of the measurement.

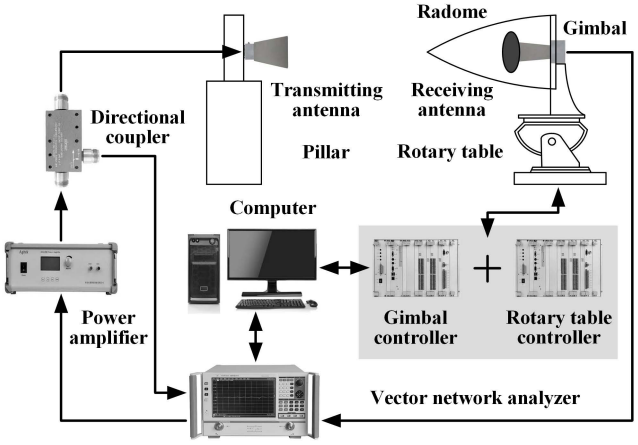

FIGURE 5. Schematic of the measurement system.

The method adopted in the measurement is called the electronic calibration method [19]. This method can be divided into three steps: 1) The transmitting antenna is fixed on the pillar. The electric axis of the receiving antenna is aligned with the electric axis of the transmitting antenna by adjusting the gimbal. 2) The receiving antenna is rotated by a series of angles without the radome. The angles and the received signals are recorded, and the calibration curve is then established. 3) The receiving antenna is realigned with the transmitting antenna and fixed. The rotary table performs the same scanning motions without and with the radome, respectively. The scanning angles and the received signals are recorded. Eventually, the measurement curves of BSE and BSES can be obtained by the calibration curve and mathematical calculations.

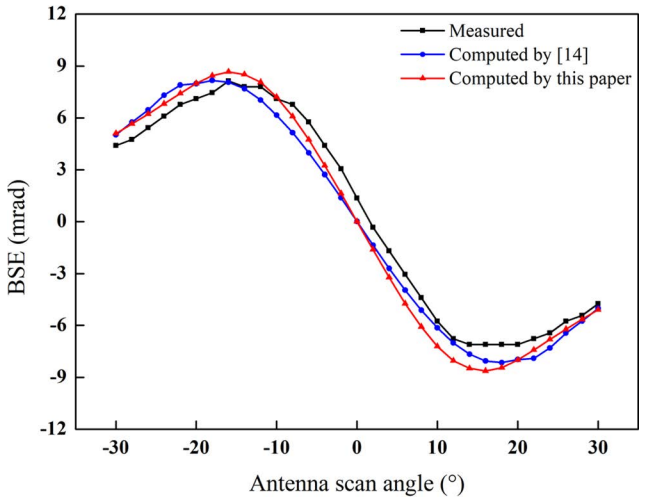

FIGURE 6. BSE comparison of measured and computed results.

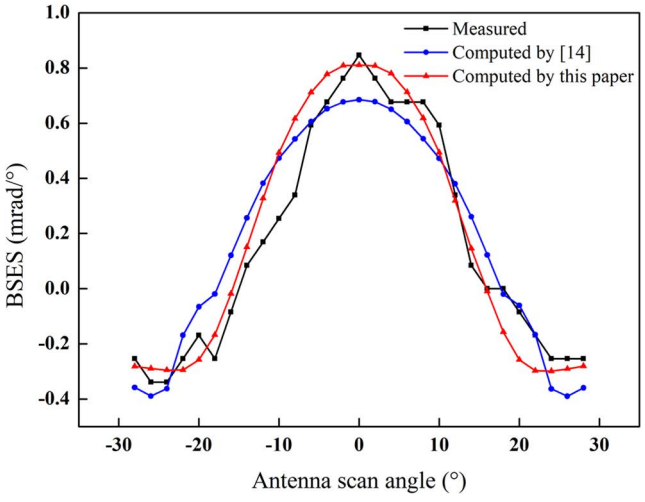

FIGURE 7. BSES comparison of measured and computed results.

It can be seen from Fig. 6 and Fig. 7 that the computed results using the proposed method are consistent with the computed results using the method proposed in [14] and the measured results.

To quantify the deviation between the computed and measured results, the errors of the EM performance parameters were calculated [20]:

$$e = \frac{\sum_{j=1}^{M} \left| A'(j) - A(j) \right|}{\sum_{j=1}^{M} |A(j)|}, \tag{9}$$

where $j = 1, \cdots, M$ is the scanning state of the antenna; $A'(j)$ is the EM performance parameter calculated using the method proposed in [14] or the one proposed in this paper, including the far-field pattern, BSE, BSES, and PT; and $A(j)$ is the corresponding measured result.

TABLE 1. Comparison of the errors and efficiencies of different methods.

	The method in [14]	The method in this paper
e_{BSE} (%)	15.89	16.69
e_{BSES} (%)	30.02	23.86
t (s)	142	40

The errors caused by the method proposed in [14] and the one proposed in this paper were calculated by using a computer with dual 2.4GHz processors (Intel Xeon). e_{BSE} is the error of BSE, e_{BSES} is the error of BSES, and t is the consumed time, as shown in Table 1.

Compared with the method proposed in [14], the method proposed in this paper has a slightly worse accuracy for BSE (an error increase of 0.8% from 15.89% to 16.69%). However, a much better accuracy for BSES can be achieved (an error reduction of 6.16% from 30.02% to 23.86%). The proposed cylindrical equivalent source-based PO method improves the computational efficiency by 71.83% (from 142s to 40s).

B. APPLICABILITY OF THE CYLINDRICAL EQUIVALENT SOURCE-BASED PO METHOD

Changing the operating frequency of the antenna-radome system means changing the electrical size of the antenna-radome system. The antenna diameter d_a was used as a reference, making it 24λ, 16λ, 10λ, and 3λ, respectively. Fig. 8 shows the far-field patterns of the enclosed antenna computed using the method proposed in [14] and the one proposed in this paper.

The errors of main lobe e_{ml} caused by the proposed method are presented in Table 2, with the results computed using the method proposed in [14] as the standard.

TABLE 2. The error of main lobe at different electrical sizes.

d_a (λ)	24	16	10	3
e_{ml} (%)	4.62	6.25	6.31	15.79

It can be seen that e_{ml} is 4.62% when d_a is 24λ, and e_{ml} gradually increases when d_a decreases. When d_a decreases to 10λ, e_{ml} increases by only 1.69% (from 4.62% to 6.31%). However, when d_a decreases to 3λ, e_{ml} increases by 11.17% (from 4.62% to 15.79%). This is due to the increase in the beamwidth, thus causing some points with relatively large fields to be not included in the cylindrical equivalent source region.

The analysis of the far-field patterns only shows the trend that the calculation error of the proposed method increases with a decrease in the electrical size. In order to determine the specific application range of electrical size of the proposed method, the operating frequency was gradually changed to reduce d_a from 24λ to 3λ. Considering BSE and PT, that are

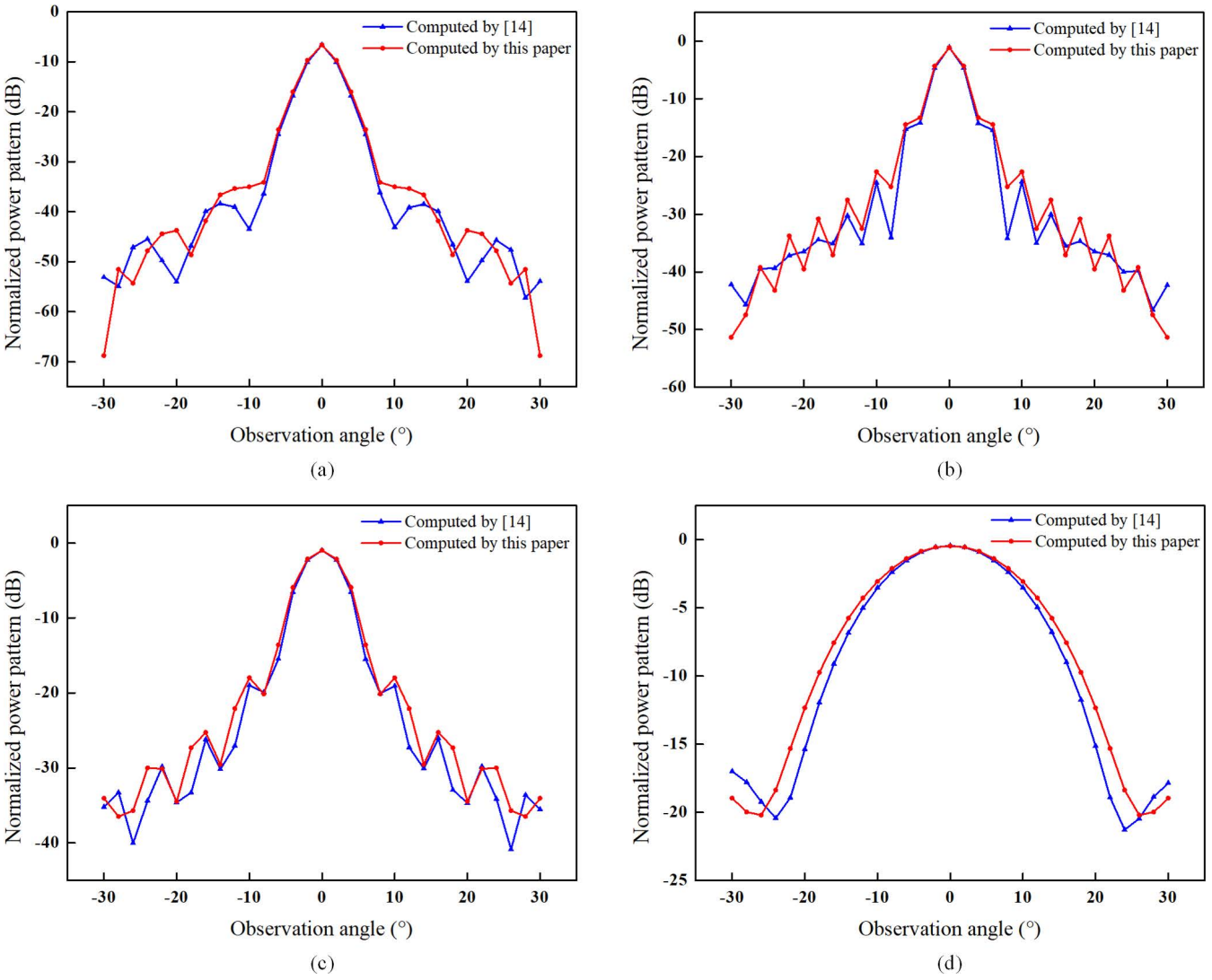

FIGURE 8. Comparison of the far-field patterns by different methods at different electrical sizes: (a) d_a is 24λ, (b) d_a is 16λ, (c) d_a is 10λ, and (d) d_a is 3λ.

two common and important EM performance parameters, the corresponding errors are illustrated in Fig. 9, where e_{BSE} is the error of BSE and e_{PT} is the error of PT. e_{BSE} gradually increases as d_a decreases. It then sharply increases when d_a is less than 4λ. e_{PT} decreases as d_a decreases, and it is small throughout the electrical size range, with a maximum value of only 3.50%.

Table 3 lists the upper limits of e_{BSE} and e_{PT} for different electrical size ranges. In the range of d_a from 24λ to 12λ, the upper limit of e_{BSE} is 10.23% and the upper limit of e_{PT} is 3.50%. In this range, the calculation results are reliable. In the range of d_a from 12λ to 4λ, the upper limit of e_{BSE} is 23.64% and the upper limit of e_{PT} is 0.77%. In this range, the accuracy of BSE becomes lower. However, the accuracy of PT becomes higher. When d_a is less than 4λ, the upper limit of e_{PT} slightly increases (from 0.77% to 0.99%). However, the upper limit of e_{BSE} sharply increases (from 23.64% to 71.28%). The reason for the sharp increase in the upper limit of e_{BSE} is consistent with the 11.17% increase in e_{ml} when d_a is 3λ. It can be deduced that BSE is the most sensitive to the reduction of the secondary source region, PT is the least sensitive, and the main lobe of the antenna is in the middle.

For the analysis of EM performance, the cylindrical equivalent source-based PO method can be applied to airborne antenna-radome systems with d_a of 12.14λ and above, if the error threshold is set to 10%. If the error threshold is relaxed to 15%, the application range of electrical size of the proposed method will be extended to 9.47λ and above. If it is relaxed to 20%, the range will be 7.61λ and above. In the actual simulation, the application range of electrical size can be determined according to the expected accuracy. The near fields of the strongly directional antennas, such as phased array antennas, are more concentrated than those of the uniformly distributed antennas. Therefore, when the same

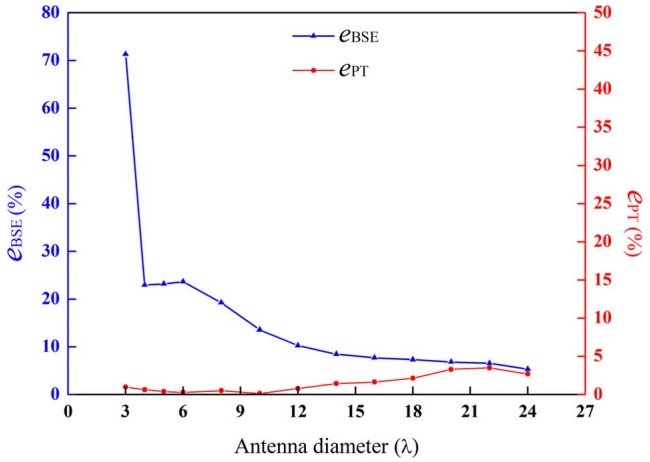

FIGURE 9. Error curves of BSE and PT.

TABLE 3. Errors of BSE and PT for different electrical size ranges.

d_a (λ)	e_{BSE} (%)	e_{PT} (%)
24-20	≤ 6.81	≤ 3.50
20-16	≤ 7.70	≤ 3.29
16-12	≤ 10.23	≤ 1.64
12-8	≤ 19.25	≤ 0.77
8-4	≤ 23.64	≤ 0.64
4-3	≤ 71.28	≤ 0.99

antenna radiation cylinder is considered, a larger portion of the secondary source points with relatively large fields is contained within the antenna radiation cylinder for the strongly directional antenna. This larger portion helps to achieve better accuracy. In other words, when the same error threshold is set, the radius of the antenna radiation cylinder for the strongly directional antenna can be smaller.

IV. CONCLUSION

This paper presents a cylindrical equivalent source-based PO method for the rapid analysis of airborne antenna-radome systems. Based on the near-field characteristics, an antenna radiation cylinder with the antenna aperture as the bottom is established. The secondary source region for far-field calculations is then reduced from the outer surface of the radome in front of the antenna to that inside the antenna radiation cylinder. Furthermore, similar mathematical models have been developed for different radomes using the cubic-spline interpolation technique, thus unifying the solution method for the boundary of the cylindrical equivalent source. The simulation results validate the effectiveness of the proposed method. Compared with the conical equivalent source-based PO method, the proposed method provides a 71.83% improvement in efficiency. Considering 10% as the error threshold, the proposed method can be applied to airborne antenna-radome systems whose antenna diameter is greater than or equal to 12.14 times of wavelength. Considering the high efficiency and acceptable accuracy, the proposed method provides a reliable numerical tool for the rapid analysis and design of airborne radomes.

REFERENCES

[1] R. Shavit, *Radome Electromagnetic Theory and Design*. Hoboken, NJ, USA: Wiley, 2018, pp. 89–143.
[2] H. Shin, D. Yoon, D.-Y. Na, and Y. B. Park, "Analysis of radome cross section of an aircraft equipped with a FSS radome," *IEEE Access*, vol. 10, pp. 33704–33712, 2022, doi: 10.1109/ACCESS.2022.3162262.
[3] H. Shin, D. Yoon, D.-Y. Na, and Y. B. Park, "Analysis of transmission loss and boresight error of a curved FSS radome-enclosed antenna," *IEEE Access*, vol. 9, pp. 95843–95852, 2021, doi: 10.1109/ACCESS.2021.3094526.
[4] A. Benini, E. Martini, S. Monni, M. C. Viganò, F. Silvestri, E. Gandini, G. Gerini, G. Toso, and S. Maci, "Phase-gradient meta-dome for increasing grating-lobe-free scan range in phased arrays," *IEEE Trans. Antennas Propag.*, vol. 66, no. 8, pp. 3973–3982, Aug. 2018, doi: 10.1109/TAP.2018.2835575.
[5] X. Yang, M. Jiang, L. Shen, P.-H. Jia, Z. Rong, Y. Chen, L. Lei, and J. Hu, "A flexible FEM-BEM-DDM for EM scattering by multiscale anisotropic objects," *IEEE Trans. Antennas Propag.*, vol. 69, no. 12, pp. 8562–8573, Dec. 2021, doi: 10.1109/TAP.2021.3091196.
[6] A. Parameswaran, H. S. Sonalikar, and D. Kundu, "Temperature-dependent electromagnetic design of inhomogeneous planar layer variable thickness radome for power transmission enhancement," *IEEE Antennas Wireless Propag. Lett.*, vol. 20, no. 8, pp. 1572–1576, Aug. 2021, doi: 10.1109/LAWP.2021.3091516.
[7] D. Paris, "Computer-aided radome analysis," *IEEE Trans. Antennas Propag.*, vol. AP-18, no. 1, pp. 7–15, Jan. 1970, doi: 10.1109/TAP.1970.1139614.
[8] D. C. Wu and R. Rudduck, "Plane wave spectrum-surface integration technique for radome analysis," *IEEE Trans. Antennas Propag.*, vol. AP-22, no. 3, pp. 497–500, May 1974, doi: 10.1109/TAP.1974.1140802.
[9] M. A. A. Moneum, Z. Shen, J. L. Volakis, and O. Graham, "Hybrid PO-MoM analysis of large axi-symmetric radomes," *IEEE Trans. Antennas Propag.*, vol. 49, no. 12, pp. 1657–1666, Dec. 2001, doi: 10.1109/8.982444.
[10] C. Gennarelli, G. Pelosi, G. Riccio, and G. Toso, "Diffraction by an anisotropic dielectric half-plane: A uniform asymptotic PO solution," *IEEE Trans. Antennas Propag.*, vol. 49, no. 12, pp. 1624–1627, Dec. 2001, doi: 10.1109/8.982438.
[11] Z. Qiang and C. Wei, "A uniform convergence technique in the surface integration of arbitrary wide-band radome," in *Proc. IEEE Antennas Propag. Soc. Int. Symp.*, Columbus, OH, USA, Jun. 2003, pp. 420–423.
[12] H. Meng, W. Dou, T. Chen, and K. Yin, "Analysis of radome using aperture integration-surface integration method with modified transmission coefficient," *J. Infr., Millim., THz Waves*, vol. 30, no. 2, pp. 199–210, Nov. 2008, doi: 10.1007/s10762-008-9438-6.
[13] A. Renuka and V. G. Borkar, "Computer-aided analysis for tangent ogive airborne radome using physical optics method," in *Proc. Asia–Pacific Microw. Conf. (APMC)*, Suzhou, China, 2005, pp. 420–423.
[14] C. Zhang, D. Guo, X. Sheng, M. Liu, and Y. Sun, "Determination of effective equivalent source for far-fields simulation of antenna in presence of radome," *J. Syst. Simul.*, vol. 21, no. 2, pp. 364–366, Jan. 2009.
[15] D. C. F. Wu, "Electromagnetic analysis of three-dimensional antenna-radomes using the plane wave spectrum-surface integration technique," Ph.D. dissertation, Dept. Electr. Eng., Ohio State Univ., Columbus, OH, USA, 1971.
[16] D. J. Kozakoff, *Analysis of Radome-Enclosed Antennas*, 2nd ed. Norwood, MA, USA: Artech House, 2010, pp. 15–33.
[17] C. Yang, Y. Peng, and Y. Zheng, "Densifying contour map based on intersecting algorithm of line and B-spline curve," *J. Syst. Simul.*, vol. 18, pp. 319–321, Aug. 2006.
[18] Y. Zhang, X. Sheng, and K. Wang, "Algorithm research on the BSE of antenna-radome system," *J. Projectiles, Rockets, Missiles Guid.*, vol. 33, no. 1, pp. 163–166, Feb. 2013, doi: 10.15892/j.cnki.djzdxb.2013.01.008.

[19] Y. Liu, "Analysis of measurement of radome boresight error by electronic calibration method," *J. Microw.*, vol. 33, no. 3, pp. 60–67, Jun. 2017, doi: 10.14183/j.cnki.1005-6122.201703013.
[20] Y. J. Zhou, "A study on integral algorithm for acceleration test to get displacement and application," M.S. thesis, Dept. Vehicle Eng., Zhongbei Univ., Taiyuan, China, 2011.

XIANJUN SHENG was born in Liaoning, China, in 1969. She received the M.S. and Ph.D. degrees from the Dalian University of Technology, Dalian, China, in 1997 and 2003, respectively.

She is currently a Professor in electrical engineering with the Dalian University of Technology. Her current research interests include reverse engineering, analysis and design of airborne radomes, computational electromagnetics, and design of artificial electromagnetic materials.

YE ZHANG was born in Liaoning, China, in 1993. He received the B.E. degree from the Dalian University of Technology, Dalian, China, in 2014, where he is currently pursuing the integrated M.E. and Ph.D. degrees in electrical engineering.

His current research interests include analysis and design of airborne radomes, computational electromagnetics, and reverse engineering.

RUI SHEN was born in Beijing, China, in 1978. She received the B.E. and M.E. degrees from the Harbin Institute of Technology, Harbin, China, in 2001 and 2013, respectively.

She is currently an Associate Director of the Industrial Control Center, China Academy of Launch Vehicle Technology, Beijing. Her current research interests include industrial control and structural design of radomes.

NING LIU was born in Liaoning, China, in 1991. He received the B.S. and Ph.D. degrees from the Dalian University of Technology, Dalian, China, in 2013 and 2019, respectively.

He is currently an Associate Professor in electrical engineering with the Dalian University of Technology. His research interests include airborne radome analysis, frequency selective surface, and reverse engineering.